Chemistry and kinematics of stars in Local Group galaxies

Battaglia, Giuseppina

Chapter 4

The DART imaging and CaT survey of the Sculptor Dwarf Spheroidal Galaxy

G. Battaglia, E. Tolstoy, A. Helmi, M. J. Irwin, P. Jablonka, V. Hill & L. Pasquini

paper in preparation

ABSTRACT– In this chapter we present the DART photometric and spectroscopic survey of the Sculptor dwarf spheroidal galaxy.
We use ESO/2.2m Wide Field Imager (ESO/WFI) photometry covering Sculptor out to and beyond its nominal tidal radius to study the spatial properties of the Sculptor stars of different ages/metallicities as selected from the Colour-Magnitude Diagram (CMD).
We obtained VLT/FLAMES low resolution (R∼6500) spectra of 1013 Red Giant Branch stars in the CaII triplet (CaT) region out to the nominal tidal radius of Sculptor. From this sample we derived accurate velocities and CaT metallicities ([Fe/H]) using the methods described in Chapter 2. This results in a sample of 470 probable Sculptor kinematic members.
We find that Sculptor stars of different metallicities have different spatial distributions and kinematic properties, with the metal rich stars being more centrally concentrated, less extended and kinematically colder than the metal poor stars.
We also find signs of rotation around the projected minor axis of Sculptor. The measured velocity gradient of $7.6^{+3.0}_{-2.2}$ km s^{-1} deg^{-1} makes the shape of Scl consistent with being flattened by rotation.

4.1 Introduction

THE Sculptor (Scl) dwarf spheroidal galaxy (dSph) is a satellite of the Milky Way (MW), located at (l, b)=(287.5°, −83.2°) and with an heliocentric distance of 79 kpc (Mateo 1998, and references therein). It is a moderately luminous dSph ($L_V = 2.15 \times 10^6\,L_\odot$), with a central surface brightness $\Sigma_{0,V} = 23.7 \pm 0.4$ mag arcsec^{-2}.

Because of the relatively close distance to the MW, Scl has received much attention as a candidate for tidal disruption. Several photometric studies have revealed a complex isophotal structure (Demers et al. 1980; Eskridge 1988a,b; Irwin & Hatzidimitriou 1995; Walcher et al. 2003; Westfall et al. 2006): the inner parts of Scl appear to be almost circular, while the isophote ellipticity increases in the outer parts. There have been claims of detections of tidal structures such as over-densities and tails (e.g., Walcher et al. 2003), however these have not been reconfirmed. At the moment there is no unambiguous evidence of tidal disruption in Scl.

Scl contains predominantly ancient stars (>10 Gyr old), as shown by a well populated Horizontal Branch (HB) and the presence of RRLyrae stars (Kaluzny et al. 1995; Clementini et al. 2005). Monkiewicz et al. (1999), using HST photometry reaching 3 magnitudes below the oldest main sequence turn-off, concluded that the age of the bulk of Scl stellar population is similar to the oldest Galactic globular clusters, and is consistent with an age spread of few Gyrs. It is unclear for how long stars formed in Scl as star formation as recent as 2 Gyr ago cannot be completely ruled out. However, until now there is no unambiguous evidence for the presence of any intermediate-age stars (2-8 Gyr old). A few candidate AGB stars have been found (Frogel et al. 1982; Azzopardi et al. 1986), although most of them might be reclassified (Shetrone et al. 1998; Groenewegen 2002). It is most likely that all stars in Scl are older than 10 Gyr.

As seen in other dSphs in the Local Group, Scl shows a radial variation of the HB morphology. This was first suggested by Hurley-Keller et al. (1999) and Majewski et al. (1999) on the basis of CMD analysis, and confirmed by Harbeck et al. (2001) and by later wide field imaging studies (Tolstoy et al. 2004, hereafter T04; Coleman et al. 2005; Westfall et al. 2006). As HB stars are known to be older than 10 Gyr, the gradient in the HB morphology is an age/metallicity gradient in the *ancient* stellar component of Scl.

There have been spectroscopic studies of individual Red Giant Branch (RGB) stars in Scl, both at low and high spectral resolution (Tolstoy et al. 2001; Shetrone et al. 2003; Tolstoy et al. 2003). These studies, which focused on the central regions, found an average metallicity of [Fe/H]= -1.5 ± 0.3 dex, and a large metallicity spread, with stars covering the range $[-2.1, -1.3]$. T04 made the first wide field combined photometric and spectroscopic survey of the Scl dSph. They found a wider metallicity range than previous studies, which is confirmed by an HR follow-up (Hill et al. 2007, in preparation; see also Chapter 2), and a spectroscopically confirmed metallicity variation with radius, with the metal rich RGB stars being more centrally concentrated than the metal poor stars. This radial variation was found to resemble the radial variation of the HB morphology, and thus the Scl metal rich RGB stars could be the lower mass counterpart of the RHB stars, and so are the metal poor RGB stars with respect to the BHB stars. This galaxy appears to have experienced a complex evolution in a short time in its early evolutionary stages.

In the light of the complexity found in the most recent works on dSphs it is now clear that studies limited to the central regions of these objects and/or to a particular population will provide an incomplete picture of these galaxies.

In this Chapter we carry out a detailed analysis of the large scale properties of the Scl dSph, benefiting from the combined information derived from our photometric and spectroscopic surveys out to and beyond Scl nominal tidal radius.

4.2 Observations and Data Reduction

4.2.1 Photometry

The photometric data presented here were acquired with the ESO/2.2m WFI at La Silla between September 2003 and September 2004. A total of 19 fields were observed. Initially we had included some archival data for the central regions in order to select targets for our early spectroscopic VLT/FLAMES observations. We also re-observed the central regions resulting in better quality data and we used these data for the final photometric catalogue, although they were not yet available for target selection.

The data reduction was done in a standard way and for the details we refer to Chapter 3 and references therein. Table 4.1 shows the journal of our WFI observations of Scl.

To find the 90% and 50% completeness limits we calculate the average magnitude of the stars with a magnitude error of 0.1 mag and 0.2 mag, respectively, in each passband. We use as a global completeness limit the magnitude of the shallowest of the completeness limits for each of the different fields. For our WFI data we find that in the V band the 50% completeness limit has a V magnitude $V_{50\%}$ =23.0 and an I magnitude $I_{50\%}$ =22.2. The 90% completeness level is $V_{90\%}$ =21.8 in the V band and $I_{90\%}$ =21.1 in the I band. In the following sections, when deriving the photometric properties of the Scl dSph, we will use the photometric sample complete at the 90%.

Table 4.1: Table of Scl ESO/WFI observations. The seeing is the average stellar FWHM from the final coadded image.

Name	Filter	UT of observation	exptime	airmass	seeing (arcsec)
SCL_25	V	20-Sep-2003 02:23	2x300s	1.4	1.68
	I		4x300s	1.3	1.00
SCL_07	V	20-Sep-2003 03:52	2x300s	1.1	0.9
	I		2x300s	1.1	0.95
SCL_32	V	20-Sep-2003 04:25	2x300s	1.0	0.86
	I		2x300s	1.0	0.88
SCL_11	V	20-Sep-2003 04:59	2x300s	1.0	0.87
	I		2x300s	1.0	0.73
SCL_05	V	20-Sep-2003 05:33	2x300s	1.0	0.83
	I		2x300s	1.0	0.78
SCL_06	V	20-Sep-2003 06:05	2x300s	1.0	0.74
	I		2x300s	1.0	0.69
SCL_08	V	20-Sep-2003 07:30	2x300s	1.1	1.10

Table 4.1: continued.

Name	Filter	UT of observation	exptime	airmass	seeing (arcsec)
	I		2x300s	1.1	1.28
SCL_02	*V*	19-Sep-2003 05:10	2x300s	1.0	0.99
	I		2x300s	1.0	0.87
SCL_03	*V*	19-Sep-2003 06:30	2x300s	1.0	0.87
	I		2x300s	1.0	0.79
SCL_04	*V*	19-Sep-2003 07:03	2x300s	1.0	1.00
	I		2x300s	1.1	0.99
SCL_14	*V*	19-Sep-2003 07:36	2x300s	1.1	0.89
	I		2x300s	1.1	0.88
SCL_09	*V*	19-Sep-2003 08:15	2x300s	1.2	1.12
	I		2x300s	1.2	1.12
SCL_17	*V*	19-Nov-2004 04:38	2x300s	1.3	0.60
	I		2x300s	1.3	0.56
SCL_20	*V*	19-Nov-2004 05:10	2x300s	1.3	0.63
	I		2x300s	1.4	0.53
SCL_10	*V*	19-Nov-2004 01:19	2x300s	1.0	0.71
	I		2x300s	1.0	0.87
SCL_12	*V*	19-Nov-2004 02:17	2x300s	1.0	0.62
	I		2x300s	1.0	0.89
SCL_13	*V*	19-Nov-2004 02:51	2x300s	1.0	0.73
	I		2x300s	1.0	1.07
SCL_14	*V*	19-Nov-2004 03:34	2x300s	1.0	0.69
	I		2x300s	1.1	0.76
SCL_15	*V*	19-Nov-2004 04:06	2x300s	1.1	0.64
	I		2x300s	1.2	0.66

4.2.2 Spectroscopy

We selected targets classified as stellar in our ESO/WFI photometry and with a position on the CMD consistent with an RGB star, but allowing a wide colour range about the RGB to avoid biasing our sample in age or metallicity. We used VLT/FLAMES feeding the GIRAFFE spectrograph in Medusa mode, that allows the simultaneous allocation of 132 fibres (including sky fibres) over a 25' diameter field of view (Pasquini et al. 2002). We used the GIRAFFE low resolution grating (LR8, resolving power R$\sim$ 6500), covering the wavelength range from 8206 Å to 9400 Å, to obtain spectra for 15 different fields in Scl dSph (see Chapter 2). We presented our initial results in T04, and with respect to the data presented there we have acquired 7 new fields.

Our data were all reduced using the GIRBLDRS* pipeline provided by the FLAMES consortium (Geneva Observatory, Blecha et al. 2003). This package provided individual spectral extraction and accurate wavelength calibration, based on daytime calibration arc exposures. The sky-subtraction and extraction of the velocities and equivalent

* available at SourceForge, http://girbldrs.sourceforg.net/

widths of CaII triplet lines were carried out using our own software developed by M. Irwin (for the details of the data reduction process see Chapter 2).

The number of independent measurements in Scl is 1740, for 1013 distinct targets. As described in Chapter 2, we checked for the reliability of our velocity and equivalent width measurements using the stars with double measurements. We find that a S/N per Å > 10 and an error in velocity < 5 km s^{-1} is the minimum for an accurate determination of velocity and equivalent width, thus we exclude from our analysis the stars that do not meet these criteria. To guarantee the reliability of the equivalent width estimate we impose as an additional selection criteria that the EW measurements coming from our gaussian and integrated flux estimators (see Chapter 2) must agree within 2 Å .

From the stars with double measurements we find that the internal velocity error (from the median absolute deviation) of our dataset is $\pm$ 2 km s^{-1} and the internal error in equivalent widths is $\pm$ 0.22 Å . The latter corresponds to an error in metallicity of $\pm$ 0.1 dex.

Finally the repeated measurements (also satisfying the signal-to-noise and velocity error criteria) were combined, weighting them by their errors. The final sample was carefully checked to weed out any spurious objects (e.g. broken fibres, background galaxies, foreground stars, etc.). We removed 4 objects because they were inadvertently assigned to fibres that were not available during our observing runs; we found no background galaxies and removed 7 objects because the continuum shape or the presence of very broad absorption line was not consistent with what is expected for RGB spectra. Our final sample of acceptable measurements consists of 648 stars for the velocities and 646 for the metallicities.

In order to investigate the possible presence of binary stars in our sample we calculate the $\chi^2_{\rm obs}$ value for those stars with multiple observations (whose individual measurements met our selection criteria) and calculate the probability of observing a larger χ^2 value by chance, $p(\chi^2 \geq \chi^2_{\rm obs})$. Following the criterion of Olszewski et al. (1996), we consider candidate binaries to be those stars for which $p(\chi^2 \geq \chi^2_{\rm obs}) \leq 0.001$. We find 6 possible binaries out of 177 stars, i.e. a possible binary fraction of 0.03, negligible for our purposes. This is a crude estimate of the binary fraction as it does not take into account the effect of the distribution of the binary orbital parameters, such as orbital inclination and period. However, previous authors (e.g., Olszewski et al. 1996; Hargreaves et al. 1996) have demonstrated that the presence of binary stars has a negligible effect on the derived velocity dispersion, especially in comparison to other sources of errors such as sampling and velocity errors. In the following analysis we therefore ignore the contribution of binaries.

4.3 Results from ESO/WFI photometry

4.3.1 Spatial structure of the Sculptor dSph

The structure of the Scl dSph has been studied in several imaging studies, which found radial changes in the ellipticity (Eskridge 1988b; Irwin & Hatzidimitriou 1995; Walcher et al. 2003; Coleman et al. 2005; Westfall et al. 2006) and an extended break population in the surface density profile of RGB/HB stars, which might hint at an

Table 4.2: Table of Scl parameters. 1. Mateo (1998) and references therein. 2. Irwin & Hatzidimitriou (1995). The position angle is defined as the angle between North and the major-axis of the galaxy measured counter-clockwise; the ellipticity is $e = 1 - b/a$.

α_{2000}	$1^h0^m09.00^s$	1
δ_{2000}	$-33°42'30''$	1
e	0.32	2
P.A.	99°	2
Distance	79 kpc	1
V_{HB}	20.13	2

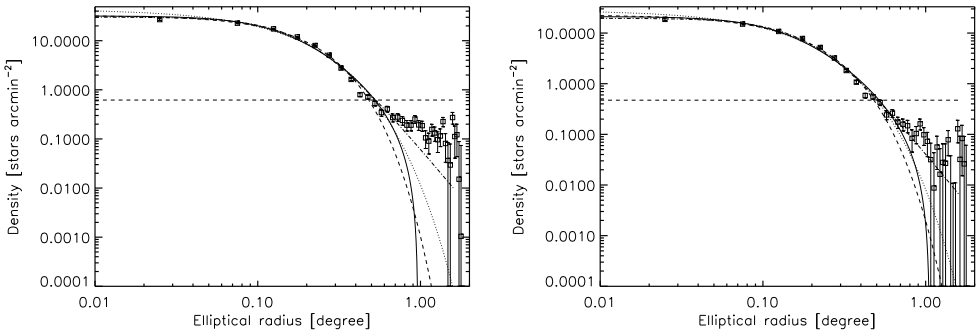

Figure 4.1: Left: The surface density profile for the Scl dSph galaxy from star counts of all the stellar objects in our photometry (squares with errorbars). The lines show the best-fitting King (solid), Sersic (dashed), exponential (dotted) and Plummer (dash-dotted) models. Right: As above but considering the stars in the 90% complete sample.

extra-tidal population, (Westfall et al. 2006). However, Coleman et al. (2005) explain this same break in the density profile without invoking tidal disruption, but by simply taking into account the different spatial distribution of the two stellar components that Scl harbours (e.g., Harbeck et al. 2001; T04).

In the following, for our analysis of the spatial structure of Scl dSph we adopt the values for the centre listed in Mateo (1998) and the ellipticity and position angle derived in IH95 (see Table 4.2).

We re-derived the surface density profile of Scl (from number counts) in bins of 0.05 deg (3 arcmin) out to 1.825 deg (109 arcmin). Though our photometry extends beyond the previously estimated tidal radius (76.5 arcmin from Irwin & Hatzidimitriou 1995, hereafter IH95), in the outer parts our coverage is not complete and homogeneous, which may cause an overestimated Galactic foreground density.

The contamination by field star density was calculate from a weighted average of the density values beyond 1.6 deg, where the density profile reaches a constant level which we can associate with the Galactic contamination density, and is 0.62 ± 0.03 stars arcmin^{-2}. The Galactic contamination-subtracted density profile that we derived for

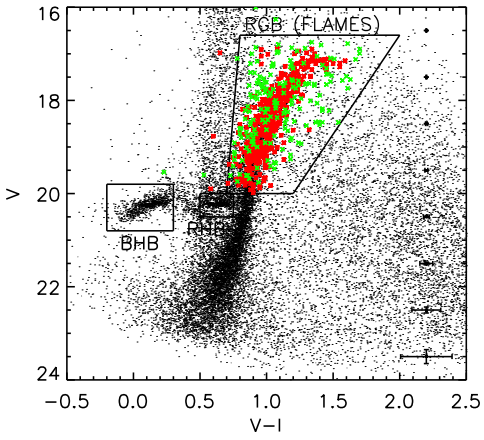

Figure 4.2: Colour-Magnitude Diagram of the Scl dSph. We show the selection boxes for deriving the spatial distribution of BHB, RHB and RGB stars. The box around the RGB follows the magnitude and colour criteria we adopted for selecting targets for our VLT/FLAMES observations. Preliminary photometry was used to select part of our FLAMES targets; the poor quality of this photometry resulted in the presence of some targets outside the selection box when compared to the accurate final WFI photometry.

all the objects classified as stellar in our photometry is shown in Fig. 4.1 (left). We compared this Galactic contamination-subtracted profile to several surface brightness models using a least-square fit to the data. We compared to an empirical King profile (King 1962), an exponential profile, a Sersic profile (Sersic 1968) and a Plummer model (Plummer 1911). For the exact form of these profiles see Chapter 3. We found that none of these profiles give a good representation of the data, as they all considerably underestimate the surface brightness at $r > 0.7$ deg (Table 4.3). Indeed at $r > 0.7$ deg the surface brightness has a shallower trend than the one predicted by the models. This corresponds to the "break population" detected by Westfall et al. (2006).

To avoid issues of saturation, completeness and varying sensitivity from one WFI pointing to another one we also re-derived the surface density profile using the photometric sample complete at the 90% level (see previous section). Figure 4.1 (right) shows the resulting surface density profile, from which we subtracted a Galactic contamination density of 0.47±0.02 stars arcmin^{-2} from a weighted average of the points beyond 1.6 deg. In this case the only profile which gives a reasonable fit to the data is a Plummer profile with I_0 =2.93 ± 0.04 stars arcmin^{-2}, b = 13.1± 0.2 arcmin. The "break population" becomes much less evident, although there is still a hint of it at $r >$ 0.7 deg. We will come back to this point in the next section. Changing the number of outer points for the determination of the Galactic foreground density has a negligible effect on the derived best-fitting model parameters.

4.3.2 The spatial distribution of different stellar populations

As already mentioned in Scl the RHB stars are more centrally concentrated and less extended than the BHB stars. We re-derive the surface number density profile for the RHB, BHB and RGB stars. The magnitude and colour criteria used to select the stars in the different evolutionary phases are shown in Fig. 4.2. These samples are more than 90% complete.

Table 4.3: Parameters of best-fitting King model (core radius, r_c, tidal radius, r_t), Sersic model (Sersic radius, R_S, shape parameter, m), exponential model (scale radius, r_s) and Plummer model (scale radius, b) for all stellar populations, all stellar populations for the sample complete at the 90% level (All 90%), RHB, BHB and RGB in the Scl dSph. For each model we also list the value of the minimum reduced χ^2. The values of core and tidal radii for the different Scl populations (RGB, RHB, BHB) are consistent with the results of Coleman et al. (2005), except for the tidal radius of the RHB component. However we point out that Coleman et al. (2005) photometry of RHB stars in not complete everywhere.

	King			Sersic			Exponential		Plummer	
	$r_c[']$	$r_t[']$	$\chi^2_{min,red}$	$R_S[']$	m	$\chi^2_{min,red}$	$r_s[']$	$\chi^2_{min,red}$	$b[']$	$\chi^2_{min,red}$
All	8.7±0.2	58.1±0.9	11.6	10.1±0.3	0.76 ± 0.02	10.3	7.3±0.1	12.1	13.0±0.2	6.7
All 90%	8.4±0.2	63.6±1.9	4.6	9.3±0.4	0.83 ± 0.03	3.9	7.4±0.1	4.4	13.1±0.2	2.2
RHB	4.9±0.4	57.2±2.7	1.9	7.7±0.9	0.74 ± 0.07	0.7	5.2±0.2	1.0	8.9±0.4	0.9
BHB	9.4±0.7	82.5±4.8	1.7	8.3±1.1	1.04 ± 0.07	2.1	9.0±0.3	2.1	15.1±0.5	1.6
RGB	7.7±0.4	69.3±4.2	2.0	8.0±0.7	0.93 ± 0.06	2.1	7.2±0.2	2.1	12.7±0.3	1.2

- **RHB stars:** We use a selection box of $20 < V < 20.5$, $0.5 < V - I < 0.75$ (see Fig. 4.2). The RHB stars are in a region of the CMD which is contaminated by Galactic foreground stars. The contamination by the field star density, from a weighted average of the surface density values at r >1.375 deg, is 0.0085 stars arcmin^{-2} *. The best-fitting model (in terms of χ^2) of the Galactic contamination-subtracted surface density profile is a Sersic, with $I_0 = 3.03 \pm 0.42$ stars arcmin^{-2}, R_S[arcmin]= 7.71 ± 0.85, m = 0.74 ± 0.07 (Fig. 4.3a). Also a Plummer model gives a good representation of the data (I_0 =0.22 ± 0.01 stars arcmin^{-2}, b = 8.9± 0.4 arcmin). In the following, we use the Sersic profile for the spatial distribution of RHB stars.

- **BHB stars:** We use a selection box of $19.8 < V < 20.8$, $-0.2 < V - I < 0.3$ (see Fig. 4.2). From the CMD we see that the BHB stars are found in a region barely contaminated by the Galactic foreground. When deriving the surface number density profile for this component we find that at r >1.6 deg the density behaviour is noisy and it is difficult to establish whether we have reached a constant density level which we can associate to the Galactic foreground density. We fit the surface number density profile in two cases: subtracting no foreground density and subtracting the foreground density derived from a weighted average of the values at r >1.6 deg, 0.0018 stars arcmin^{-2}. In each case, the best-fitting model is a Plummer profile, with I_0 =0.35 ± 0.01 stars arcmin^{-2}, b = 15.5± 0.5 arcmin (no foreground), and I_0 =0.34 ± 0.01 stars arcmin^{-2}, b = 15.1± 0.5 arcmin (foreground=0.0018 stars arcmin^{-2}). There is no significant difference in the derived parameters for the two cases. In the following we adopt the values from the foreground subtracted fit (see Fig. 4.3b).

* the use of a different region does not change the best-fitting parameters or the best-fitting model significantly, within the errors.

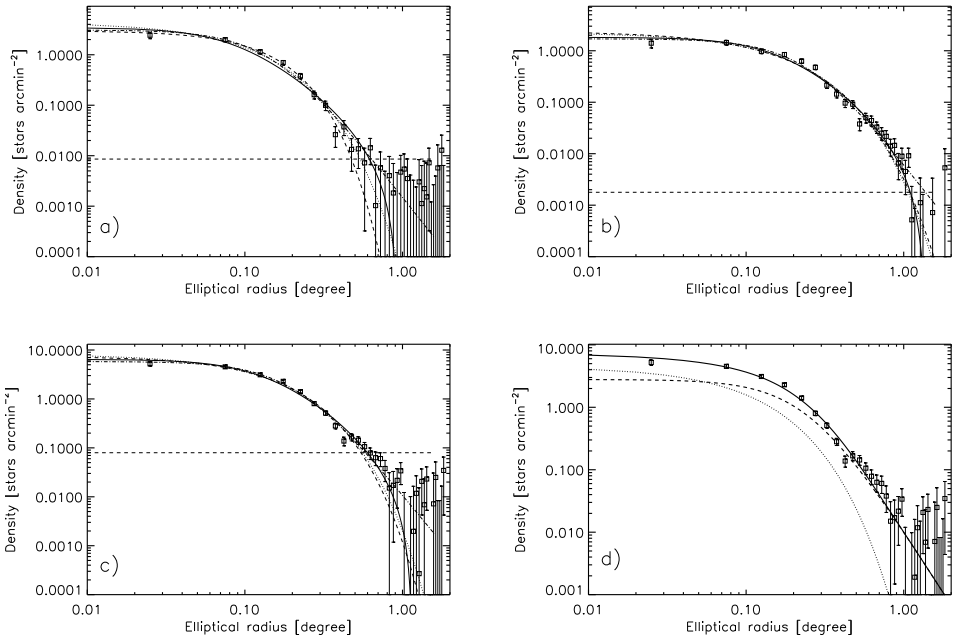

Figure 4.3: The surface density profile for Scl dSph from star counts (squares with errorbars), with overlaid best-fitting King (solid), Sersic (dashed), exponential (dotted) and Plummer (dash-dotted) models for RHB (a), BHB (b), and RGB stars (c). The Galactic stellar contamination (different in each of the panels) was calculated from a weighted average of the outermost points and has been subtracted from each point. The errorbars are obtained by summing in quadrature the errors from Poisson statistics and the error in Galactic foreground density. The best-fitting parameters are summarised in Table 4.3. Panel d) shows the surface density profile for RGB stars (squares with errorbars) overlaid to the best-fitting two component model (solid line) given by the sum of a Sersic (dotted line) and a Plummer (dashed line) profile.

- **RGB stars:** The RGB stars are the less evolved counterpart of the HB stars, both RHB and BHB. Their spatial distribution is thus expected to be intermediate between the distributions of the HB components. The RGB profile is determined from a selection box which has magnitudes and colour similar to the one used for the VLT/FLAMES targets selection (Fig. 4.2). The foreground density we derive at r >1.6 deg is 0.08 stars arcmin^{-2}. The best-fitting profile is a Plummer model, with I_0 =0.82 ± 0.02 stars arcmin^{-2}, b = 12.7± 0.3 arcmin (Fig. 4.3c). We check that our determination of the Galactic foreground density is appropriate by comparing our derived value to the Galactic foreground density predicted by Besançon model (Robin et al. 2003) over an area similar to the area covered by our photometry and in the same CMD region used for the RGB stars. The two values agree well with each other, with the Besançon model predicting ∼10% more foreground.

We saw in Sect. 4.3.1 that the overall density distribution of Scl is not well represented by a single component fit; this is because of an extended "break population" found in the outer parts. We find that a two-component fit to the overall density distribution (stars in the 90% complete sample), where the two components have the same shape of the best-fitting profiles for RHB and BHB stars, gives a reasonable representation of the data. This also applies to the distribution of RGB stars, confirming the result of Coleman et al. (2005). Figure 4.3d shows the composite fit to the RGB density profile. We point out that "break populations" should not necessarily be interpreted as signs of tidal disturbance, in particular in galaxies with distinct stellar components that are differently distributed. A summary of the best-fitting results presented in this Section is given in Table 4.3.

With the above analysis we confirm that the spatial distribution of RHB stars is more centrally concentrated and less extended than the one of BHB stars, in agreement with previous works (e.g., Harbeck et al. 2001; T04; Coleman et al. 2005; Westfall et al. 2006). This implies a complex early (> 10 Gyr ago) evolution for Scl. This is somewhat different from our finding in Fnx (Chapter 3), where all the ancient stars (> 10 Gyr old) exhibit the same extended spatial distribution.

4.3.3 Contour maps

Maps of the 2D distribution of iso-density regions in a galaxy can be used to explore its morphology. They can, in particular, point out radial variations in the ellipticity and position angle, and show the presence of over/under-dense regions. Also indications as to the dynamical status of the objects can be inferred from these maps, for example "S-shaped" contours might indicate tidal disruption (or triaxiality).

From the contour plots shown in Figure 4.4a,b we confirm the previously observed radial change in the ellipticity of Scl contours, with the inner contours being rounder than the outermost. However, the region of 3σ significance above the foreground contamination is restricted to $r < 0.8$ deg and at larger radii it becomes difficult to separate Scl from the foreground. We do not detect any clear extension in the North-East direction which was found in some previous works, nor any signs of tidal disturbance such as "S-shaped" contours.

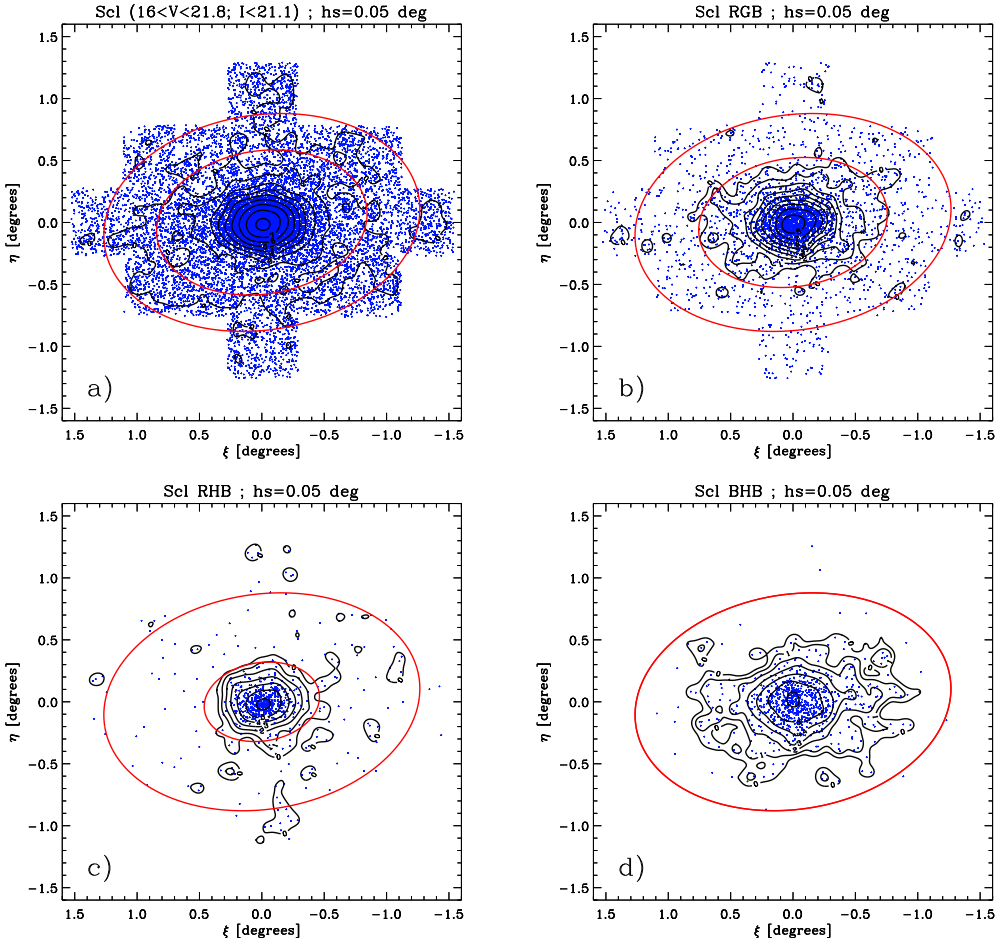

Figure 4.4: Contour maps of stellar distribution in Scl for the stars in the 90% complete sample (a), RGB stars (b), RHB (c) and BHB stars (d). Each star was convolved with a unit-normalised Gaussian of width 0.05 deg (3 arcmin). The outermost ellipse shows the nominal tidal radius (IH95); the inner ellipse indicates the radius where the density (not foreground subtracted) is 3σ times the foreground density. The first contour is chosen to be approximately contained within the region with density 3σ above the foreground. Each contour indicates a density equal to the 1.5 (a,b) or 2 (c,d) times the previous contour. We overplot the individual stars in each sample to highlight the features of the observed spatial distributions, as well the small number statistics.

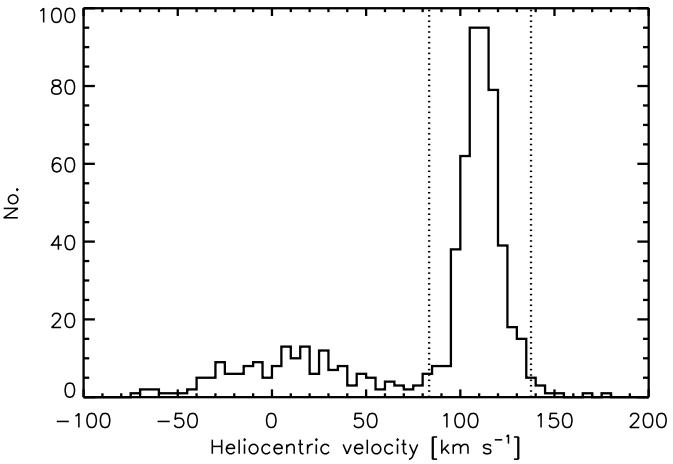

Figure 4.5: Distribution of heliocentric velocities for all the stars observed with VLT/FLAMES in the direction of the Scl dSph (648 stars, with S/N per Å>10 and error in velocity < 5 km s^{-1}) and with V magnitude and $V-I$ colour consistent with RGB stars. The dotted lines indicate the region used for the 3-σ membership selection.

We also attempted a separate analysis of the maps of RHB and BHB stars. Figure 4.4c,d suggest that the BHB stars have a more flattened distribution than RHB stars as the latter have more circular contours. However, comparing the distributions at similar radii we do not see significant differences. It is clear from the plots that definitive conclusions are hampered by small number statistics.

From this test we conclude that Scl does not show evident signs of tidal disturbance in its morphology, only that blue (older) HB stars are less centrally concentrated than red (younger) HB stars.

4.4 Results from VLT/FLAMES spectroscopy

From our VLT/FLAMES spectroscopic survey of individual stars in the Scl dSph we derived accurate velocities and metallicities ([Fe/H]) from the CaT equivalent width for 648 and 646 RGB stars, respectively. Hereafter we will use in our analysis only these stars. We refer to Chapter 2 for the details regarding the calibration and validity of metallicities derived from the CaT method.

4.4.1 Systemic velocity and global velocity dispersion

Figure 4.5 shows the velocity histogram of the VLT/FLAMES observations which passed our quality selection criteria. We derive the systemic velocity and velocity dispersion of Scl using an iterative k-σ clipping procedure. We first calculate the weighted average velocity and dispersion for the stars within 4σ of the velocity peak associated with Scl, using as a first guess a dispersion σ =15 km s^{-1}, until the values converge. We repeat the procedure restricting the k-σ range of selection. From the 3-σ clipping we find a systemic velocity $v_{\rm sys} = 110.6 \pm 0.5$ km s^{-1} and a line-of-sight (l.o.s.) dispersion $\sigma_{\rm los} = 10.1 \pm 0.3$ km s^{-1}. This is in good agreement with the value found by Queloz et al. 1995 ($v_{\rm sys} = 109.9 \pm 1.4$ km s^{-1}), and in 2σ agreement with the value from Westfall et al. (2006), $v_{\rm sys} = 107.96 \pm 0.76$ km s^{-1}. Note that our velocity

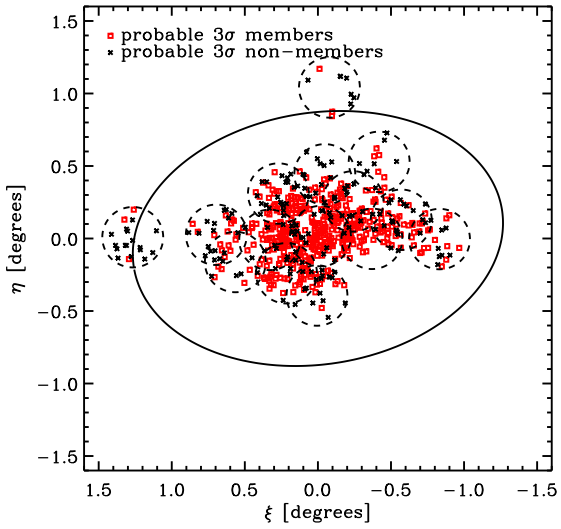

Figure 4.6: Location of the observed VLT/FLAMES fields (dashed circles) and targets in the Scl dSph (squares: probable members within 3σ of systemic velocity; crosses: probable non-members, beyond 3σ of systemic velocity). The ellipse shows the nominal tidal radius (value from IH95); the dashed circles indicate the observed FLAMES fields.

resolution is better than in Westfall et al. (2006) and with lower errors. A simple 3-σ selection of our measurements results in 470 probable Scl members. The location of these probable members and non-members is shown in Fig. 4.6.

4.4.2 Metallicity distribution

We have already shown that there is a radial variation of the metallicity properties of the RGB stars in the Scl dSph, with the metal rich stars being more centrally concentrated than the metal poor stars (T04). In this work we add additional fields, update and improve this earlier result, using the calibration derived in Chapter 2 for deriving metallicities from the CaT EW. Figure 4.7 shows the Scl metallicity distribution. Scl stars cover a large range of metallicities, from $-3.0 \lesssim$ [Fe/H] $\lesssim -0.8$. In the region $r \lesssim 0.2$ deg stars covering the full [Fe/H] range are found, whilst at larger distances we find preferably stars with [Fe/H]$\lesssim -1.6$. This confirms the trend shown in T04, and adopting the new metallicity calibration has a negligible difference with respect to that used by T04.

The overall metallicity distribution is shown in Fig. 4.8 and is reasonably approximated by the sum of two Gaussians, one representing the metal-rich (MR) part of the distribution and the other one the metal-poor (MP) part. In this case the MR component peaks at [Fe/H]~ -1.5 with a dispersion of 0.2 dex, and the MP component peaks at [Fe/H]~ -2.0 with a dispersion of 0.26 dex. From Fig. 4.8 we also see that MP stars represent the bulk of the Scl RGB population.

Finally we note that the typical metallicity errors for these observations are of order 0.15 dex (see Chapter 2), thus metallicity errors alone do not account for the observed spread in metallicity of the two components. This is in contrast with the suggestion of two almost mono-metallicity components (Majewski et al. 1999), although the predicted [Fe/H] for these two components is consistent with the [Fe/H] peaks of the MR and

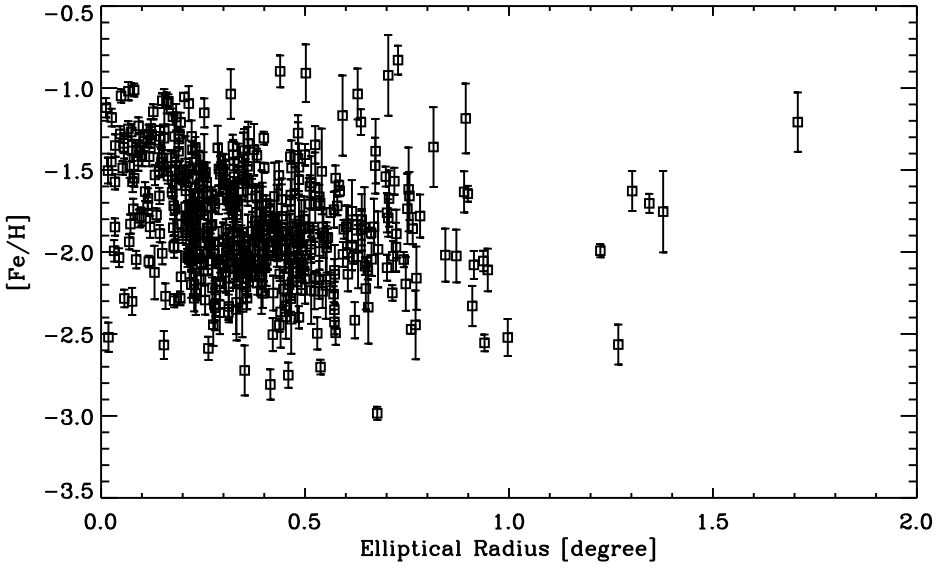

Figure 4.7: Metallicity distribution as function of elliptical radius of the Scl 3σ members (squares with errorbars). We use the metallicity calibration derived in Chapter 2. The stars with [Fe/H]> -1.5 found at $r \gtrsim 0.5$ deg are likely to be Milky Way contaminants (see Chapter 5).

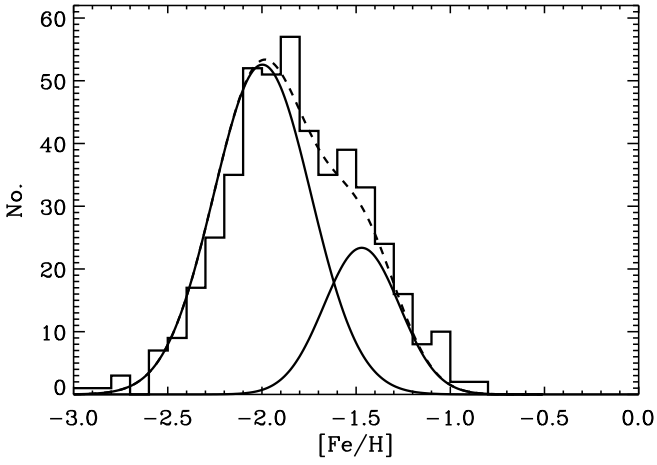

Figure 4.8: Metallicity distribution function for Scl 3σ members (histogram). The solid lines show the two best-fitting gaussians which approximate the MR and MP component, while the dashed line shows their sum.

MP stars distributions found in this work.

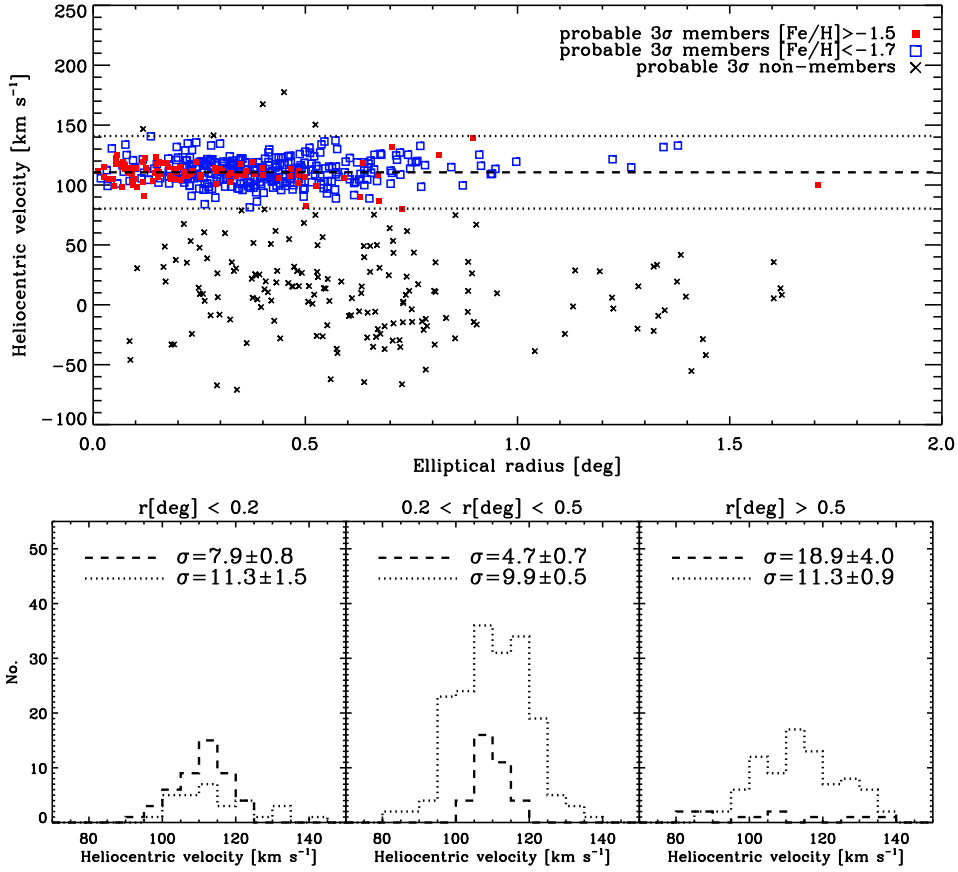

Figure 4.9: As previous figure but the MR stars are defined as those with [Fe/H]$>$ -1.5 and the MP stars with [Fe/H]$<$ -1.7. Note the colder kinematics of MR stars with respect to the MP stars, indicated by the values of the velocity dispersion. In the next chapter we will see that the MR stars present in the bin at $r > 0.5$ deg are very likely to be contaminants from the Milky Way, causing the high value of the velocity dispersion.

4.4.3 Chemo-dynamics

We have shown that Scl RGB stars of different metallicity have a different kinematic behaviour, with the MR stars being kinematically colder than the metal poor stars (T04). Here we quantify the behaviour of Scl stars of different metallicities by examining the kinematics of MR and MP stars.

As shown in Fig. 4.8 the two Gaussians representing the MR and MP stars cross at [Fe/H]~ -1.6 and have a large metallicity range of overlap.

Thus, it is likely that the two components may contaminate each others kinematics. This is especially true for the MR stars, which are outnumbered by the MP stars at $r \gtrsim 0.2$ deg. We thus need to try and minimise this contamination. As a compromise between avoiding the largest region of overlap and still having a reasonably large number of stars in each of the two components, hereafter we define as MR the stars with [Fe/H]> -1.5 and as MP the stars with [Fe/H]< -1.7. At [Fe/H]~ -1.5 the ratio between the number of MR versus MP stars, $N_{\rm MR}/N_{\rm MP}$, is 0.6 and so is $N_{\rm MP}/N_{\rm MR}$ at [Fe/H]~ -1.7; the two ratios quickly increase within the mentioned metallicity ranges. From Fig. 4.9 we see that the velocity dispersion of the MR stars is distinctly different and colder than the MP stars at radii $r < 0.5$ deg, confirming the preliminary findings of T04.

The exception to the above trend is the last bin. Fig. 4.10 may explain the reason for this: the [Fe/H] versus velocity plot shows that the vast majority of the stars found outside the 3σ membership selection region, and hence most likely to be foreground contamination from the MW, are preferentially found in the range $-2.1 \lesssim$ [Fe/H] $\lesssim -0.7$. According to their CaT metallicity value 50% of these contaminants have [Fe/H] > -1.5 and are therefore classified as MR, and just 20% have [Fe/H] < -1.7 and are classified as MP. This means that the MR stars in Scl are more likely to be contaminated by MW stars whose velocity happens to fall in the membership velocity selection region, in particular in the outer parts where the foreground to Scl members ratio becomes more significant. We will examine this issue further in Chapter 5.

In summary, our data show that Scl hosts two kinematically distinct components, one peaking at [Fe/H]~ -1.5 less extended and with colder kinematics than the other component peaking at [Fe/H]~ -2.0. Also in Fnx the MR stars have a less extended spatial distribution and a colder dispersion than the MP stars, however unlike in Scl, the bulk of stars in Fnx is MR (see Chapter 3).

4.4.4 Velocity substructure

Another feature visible in the velocity versus projected radius diagram (e.g., Fig. 4.9) is the presence of a group of 17 stars with $0.2 \lesssim r \lesssim 0.6$ deg, clustering around an heliocentric velocity of 133 km s^{-1} (between 128 km s^{-1} and 142 km s^{-1}). This group of stars exhibits a particularly low velocity dispersion, 2.4 ± 0.7 km s^{-1} .

The spatial distribution of these stars is shown in Fig. 4.11 (top). They are spread over the inner region of Scl, unlike the cold kinematic structures in Ursa Minor (Kleyna et al. 2003) and in Sextans (Walker et al. 2006b) which are more localised.

Their metallicity distribution is also shown in Fig. 4.11 (bottom) and compared to the global metallicity distribution of Scl. Considered all together, the stars in the "substructure" cover quite a large range in [Fe/H], from $-2.8 \lesssim$ [Fe/H] $\lesssim -1.6$. If we consider separately the stars at $0.2 < r < 0.3$ deg, we see that this group of stars shows a much narrower metallicity range, with an average [Fe/H]$= -1.96 \pm 0.05$ and a spread of 0.08 ± 0.06 dex, lower than the typical metallicity error for the sample of Scl stars. Such a narrow [Fe/H] and low velocity dispersion could indicate that these stars belong to a dissolved stellar cluster.

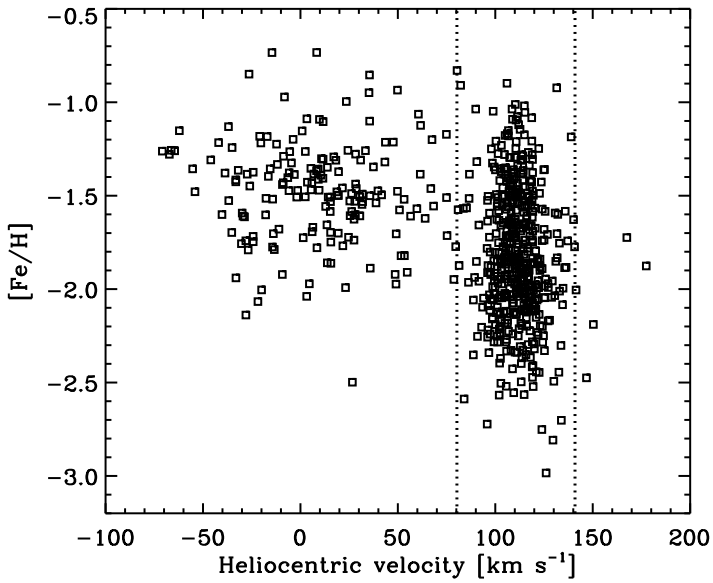

Figure 4.10: [Fe/H] versus heliocentric velocity for the observed VLT/FLAMES targets. The dotted lines indicate the region where most likely Scl members are to be found (3σ membership region). Note that the stars found outside this region, which are probable Galactic contaminants, tend to be preferentially found in the range $-2.1 \lesssim$ [Fe/H] $\lesssim -0.7$. This means that Scl stars at [Fe/H]$\lesssim -2.1$ are less likely to be contaminated by Galactic stars whose velocity falls in the 3σ membership selection region.

To test if this detection is statistically significant we calculated the expected number of stars at those radii and velocities, assuming that the stars are drawn from a Gaussian distribution centred around the measured Scl systemic velocity $v_{\rm sys}$ and with dispersion given by the measured Scl dispersion at $0.2 < r < 0.3$ and at $0.3 < r < 0.6$ deg from a 2σ selection (7.7 and 9.2 km s^{-1} respectively), which excludes the stars in the "substructure". The expected number of stars is 1.2±1.1 and 6.1±2.5. Thus we have approximately 7 stars in excess at $0.2 < r < 0.3$ deg, and 3 at $0.3 < r < 0.6$ deg, implying that in the latter bin the observed number of stars is consistent with being drawn from the main Scl population.

Therefore, the only significant detection appears to be for the stars found at $0.2 < r < 0.3$ deg, which are those that show a narrow [Fe/H] range. Assuming that the ratio of these excess stars to the total number of Scl members (7/470) is representative, then the stars in the substructure would be 1.5% of the overall Scl population. Assuming a total Scl V luminosity $L_V = 2.15 \times 10^6\,{\rm L}_\odot$ (Mateo 1998) and a stellar mass-to-light $(M/L)_{lum,V}$ =2 typical of globular clusters (Illingworth 1976; Pryor et al. 1988) and thus plausible for an old stellar population such that of Scl, crude estimates of the possible total luminosity and mass of this structure are $\sim 3.2 \times 10^4\,{\rm L}_\odot$ and $\sim 6.4 \times 10^4$

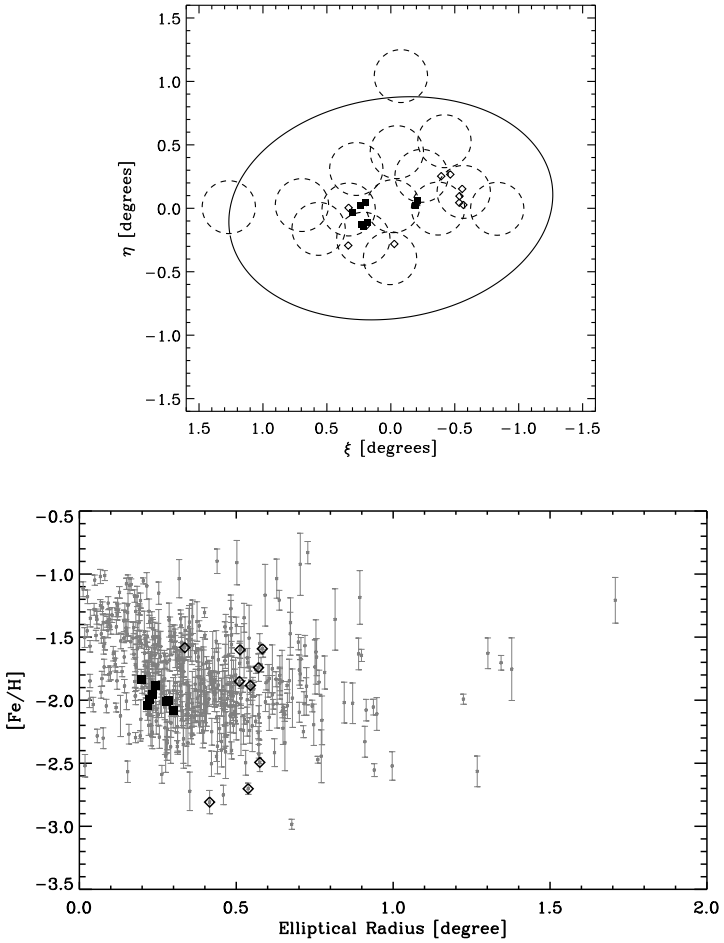

Figure 4.11: Top: Location of the stars found in a cold structure at $0.2 \lesssim r \lesssim 0.6$ deg centred at heliocentric velocity between 128 and 142 km s^{-1}. The ellipse shows the nominal Scl tidal radius (IH95) and the dashed circles the location of our VLT/FLAMES pointings. Bottom: Metallicity distribution of Scl 3σ probable members with elliptical radius (small squares with errorbars). The larger filled squares and open diamonds indicate the stars found in the velocity substructure at $0.2 \lesssim r \lesssim 0.3$ deg and $0.3 \lesssim r \lesssim 0.6$ deg, respectively.

$M_\odot$, respectively. This is of the same order of the luminosity and mass that Kleyna et al. (2003) and Walker et al. (2006b) derived for the cold-structures in Ursa Minor and Sextans, respectively. This luminosity corresponds to an absolute $M_V = -6.4$, which is similar to globular clusters found in the Fnx dSph and in other dwarf galaxies (e.g., see van den Bergh 2006).

It should be noted that the [Fe/H] values are calculated assuming that the stars in the "substructure" are at the same distance of Scl. If these stars are actually an external feature, then the [Fe/H] derived here are unlikely to be correct.

4.4.5 Kinematic status and rotation

There has been an ongoing debate as to whether the large velocity dispersion values measured for dSphs are due to large amounts of dark matter present in these galaxies, or if they are merely the result of tidal heating by the Milky Way. It has been proposed that dSphs do not contain any dark matter and that they are being tidally disrupted by the interaction with the potential of the host galaxy (e.g., Kroupa 1997; Klessen & Kroupa 1998). This model predicts tidal tails extending for several kpc, that should be detectable, for instance via the broadening of the horizontal branch in the CMD. This has not been seen in any of the dSphs satellites of the Milky Way. Another prediction of this kind of models is the presence of "apparent rotation", i.e. a velocity gradient should be detectable in the outer parts of dSphs (outside the "true" tidal radius) along the azimuthal direction of the galaxy's motion (e.g., Oh et al. 1995; Klessen & Zhao 2002). The expected l.o.s. velocity gradient is predicted to be about 20 km s^{-1} deg^{-1} (Klessen & Zhao 2002).

Another factor that could inflate the measured velocity dispersion is actual rotation. However detecting rotation in dSphs might be hampered by large velocity errors, a low $v_{\rm rot}/\sigma$ ratio and the lack of (or partial) coverage at large radii. A low $v_{\rm rot}/\sigma$ would make it difficult to distinguish a rotation signal from the "noise" caused by the large dispersion. Large velocity errors would have the same effect. Furthermore, if we compare with rotation curve studies in low surface brightness galaxies or in dEs in the Virgo cluster of galaxies (e.g., Geha et al. 2003), we expect a slowly rising rotation curve for low luminosity galaxies such as dSphs. Detecting such a rotation signal would thus require good coverage of the outermost regions. For many years studies of these galaxies have focused only on the central regions, and even now that the outer regions are starting to be considered, the number of stars at large distance from the centre still remains low due to the complexity of distinguishing members from the dominant foreground population. Marginal rotation has been detected in Ursa Minor, Draco and LeoII (Hargreaves et al. 1994, 1996; Wilkinson et al. 2004; Koch et al. 2007a). Carina is the only dSph which shows a statistically significant signal, which has been interpreted as a sign of tidal disruption (Muñoz et al. 2006).

Here we test for the presence of (an apparent or real) rotation signal in our dataset of Scl stars.

As the signal, if present, is likely to be of order a few km s^{-1}, for the following tests we use the velocity in the Galactic Standard of Rest (GSR) frame, $v_{\rm GSR}$. This is to avoid introducing spurious gradients from the component of the Solar motion and Local Standard of Rest (LSR) along the line-of-sight to Scl stars.

The Galactic Standard of Rest velocity is related to the heliocentric velocity $v_{\rm h}(l,b)$ by

$$v_{\rm GSR}(l,b) = v_{\rm h}(l,b) + v_{\odot}(l,b) + v_{\rm LSR}(l,b) \tag{4.1}$$

where $v_{\odot}(l,b)$ is the Solar motion along the line of sight and $v_{\rm LSR}(l,b)$ is the LSR velocity along the line-of-sight (see Binney & Tremaine 1987, for extended formula). We use

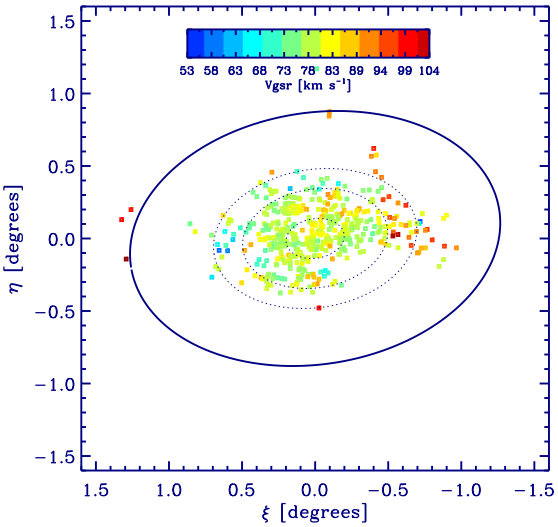

Figure 4.12: Velocity field for the Scl dSph. The velocities of individual stars were corrected for the Solar and LSR motion along the line of sight to each star. The velocity field was smoothed with a median filter. The colorbar indicates the velocity scale. The dotted ellipses are placed at 0.2, 0.5, 0.7 deg to give an idea of the distance scale. The solid ellipse shows the nominal tidal radius (from IH95).

$v_{\rm LSR}$ =220 km s^{-1} , and a Solar motion (U,V,W)=(−10.00, 5.25, 7.17) km s^{-1} (Dehnen & Binney 1998), i.e. $v_\odot$ =13.38 km s^{-1} in the direction (l, b)=(27.7°, 32.4°). In this system the systemic velocity of Scl is $v_{\rm sys,GSR}$ = 78.3 km s^{-1} .

2D maps

We built a 2D velocity field of Scl dSph to look for signs of rotation everywhere in the galaxy. We applied a median smoothing to the data to remove small scale variations. In practise, for each star we replaced its velocity with the median velocity of neighbouring stars with coordinates (ξ, η) falling in a square of side 0.1 deg centred on the star.

Figure 4.12 shows the velocity field obtained for the $v_{\rm GSR}$ of 3σ members. We find hints of rotation, as there is a concentration of stars with velocity lower than the systemic located at ∼(0.6 deg, −0.1 deg) and higher than the systemic at ∼(0.6 deg, +0.1 deg), thus approximately along the major axis. Because of the present distribution of measurements is difficult to distinguish a clear rotation pattern purely from this diagram. More data covering the whole region along the tidal radius would be desirable.

Using the most recent of the proper motion measurements for the Scl dSph (Schweitzer et al. 1995; Piatek et al. 2006) we also checked that the contribution of the bulk motion of Scl along the line-of-sight of each Scl star has a negligible effect on the measured velocities, and hence on the detected rotation signal.

Rotation signal

We will now attempt to quantify the signatures of rotation visible in Fig. 4.12 in a statistically robust way.

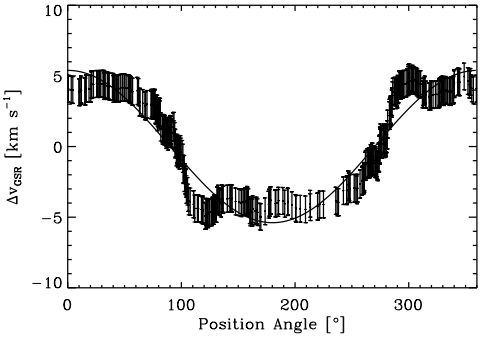

Figure 4.13: Difference of average velocity for the two halves of the Scl dSph bisected by a line having the position angle of each star, versus the position angle. The error-bars are from the errors in the average velocity measurements. The velocities were corrected for Solar and LSR motion.

- We bisect the field of view of Scl with lines having the position angle of each of the stars and calculate the average $v_{\rm GSR}$ for the two halves of the galaxy, as done in Walker et al. (2006a) for the Fornax (Fnx) dSph. The difference in the average velocity of the two halves is plotted against the position angle (Fig.4.13). If Scl rotated as a rigid body, the trend of the average difference in velocity with position angle is expected to be a sine function, with an amplitude approximately twice the rotational speed and with a phase given by the projected axis of rotation. With the present spatial coverage of measurements, the resulting velocity field makes it difficult to assess if Scl is rotating as a rigid body or not, thus the parameters of the fitted sinusoid will just give an indication of the magnitude of the rotation signal and its direction. The velocities in the GSR system give a "rotational speed", $\sim 2.70 \pm 0.04$ km s^{-1}, with a preferred projected axis of rotation of $\sim 0.2 \pm 0.6°$, close to Scl minor axis (P.A.$= 9°$).

  We test for the significance of this rotational signal by simulating 10^4 sets of 470 stars (number of 3σ members) with positions as observed and velocities randomly drawn from a Gaussian distribution of $\sigma = 10.1$ km s^{-1}, allowing for an error in velocity of 2 km s^{-1}. We find that none of the simulated datasets produce an amplitude as large as the one measured in the observations. However the trend of the velocity difference versus position angle in the mock sets is often far from being a sine function, so when we refer to an amplitude we mean the maximum value of the velocity difference. This test tells us that our data are consistent with a rotation signal around the minor axis of Scl dSph.

- We now analyse the velocity trend of stars falling within "slits" along axes with pre-established position angles (see Fig. 4.14).

  Figure 4.15 shows the observed velocity trend of Scl stars falling in the above "slits". In each case we plot the median velocity per distance bin using a constant number of stars per bin (N$\sim$30). We use the median instead of the average because it is less sensitive to substructures and asymmetries in the velocity distribution.

  We find that the only detectable signal is along the major axis (4.15c), where at $r \sim -0.7$ deg the median velocity is larger than the systemic and at $r \sim +0.5$

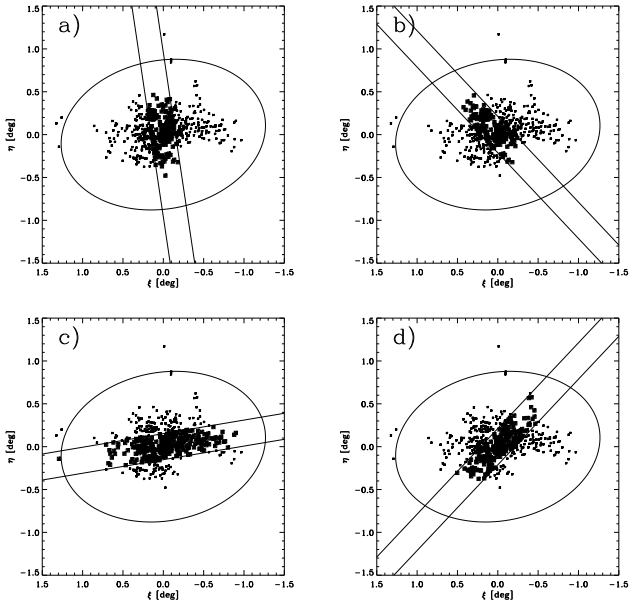

Figure 4.14: Selection regions (within the two solid lines) for stars along the minor axis (a), an axis with P.A.= 45° (b), the major axis (c), an axis with P.A.= 135° (d). The North is up ($\eta > 0$) and the East is on the left side ($\xi > 0$). Figure 4.15 shows the velocity trend with distance of the Scl probable members which fall in the above selection regions.

we see the opposite behaviour. This signal is consistent both with a straight-line and with a constant mean velocity in the central regions and a variation in the outer parts. The best-fitting straight-line gives a velocity gradient of $7.6^{+3.0}_{-2.2}$ km s^{-1} deg^{-1}. The error on this gradient has been derived from fitting 1000 mock velocity datasets created by drawing the velocities from Gaussians centred on the observed $v_{\rm GSR}$ with dispersion given by the measured velocity error and the measured Scl dispersion (i.e. $\sigma_{\rm los} = 10.1$ km s^{-1}).

Along the other "slits", the trend of the median velocity per bin is consistent with no radial variation. We also investigate if the stars identified in Sect. 4.4.4 as a possible substructure might affect the velocity trend. We find that removing these stars has a negligible effect on the results.

We repeated the same test dividing our sample in MR and MP stars. The MR stars do not show any sign of rotation neither along the major nor the minor axis. The MP stars reflect the overall behaviour, thus a rotation signal consistent with zero within ±0.5 deg and visible at larger distances. Taking into account that MR stars have a less extended spatial distribution than MP stars, we conclude that there is no conclusive evidence that MR and MP stars show different rotation patterns.

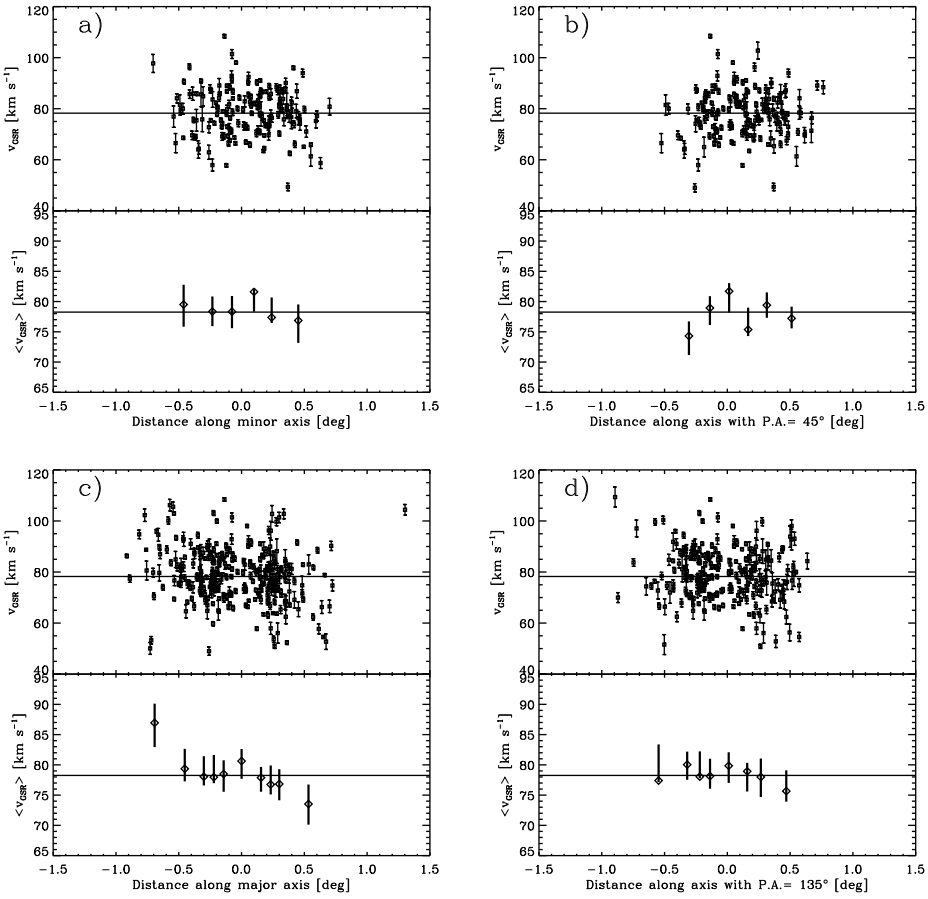

Figure 4.15: Galactic Standard of Rest velocity ($v_{\rm GSR}$) versus elliptical distance (squares with errorbars) for Scl 3σ members which fall on a selection region along the minor axis (a), an axis with P.A.= 45° (b), the major axis (c), an axis with P.A.= 135° (d). The selection regions are shown in Fig. 4.14. The bottom panels of a), b), c), d) show the median $v_{\rm GSR}$ per bin (diamonds with errorbars). Each bin contains 30 stars, except in the last bin (with the most negative distance), which has 16(a), 19(b), 21(c) and 24(d) stars. The errorbars on the median come from 10000 MonteCarlo realisations of the observed dataset, assigning an intrinsic dispersion of 10.1 km s^{-1} . The solid lines show the systemic velocity in the GSR reference frame, $v_{\rm sys,GSR}$ =78.3 km s^{-1} . Along the major axis positive distances correspond to the east side of the galaxy, negative distances to the west side.

Therefore our data are consistent with a velocity gradient of $7.6^{+3.0}_{-2.2}$ km s^{-1} deg^{-1} ($\sim$5.4 $^{+2.2}_{-1.5}$ km s^{-1} kpc^{-1}) along the projected major axis of Scl. This signal is consistent with the previous derivation from bisecting the face of the galaxy in halves. We interpret this signal as actual rotation around Scl projected minor axis and not as a sign of tidal disruption. We discuss the reasons for our favourite interpretation in the next section.

4.5 Discussion

4.5.1 Rotation signal

Our VLT/FLAMES survey of the Scl dwarf spheroidal galaxy shows that a rotation signal is present along the major axis, which could arguably be consistent both with tidal disruption and/or actual rotation.

There are a number of reasons to argue against tidal disruption. A clear sign of tidal disruption is the presence of "S-shaped" contours in the spatial distribution of the stars due to the presence of tidal tails. The tidal tails are usually perpendicular to the main body of the galaxy and in general aligned with the orbital motion of the satellite, so in principle we would not detect them if the tidal tails are (close to) either perpendicular or parallel to our line-of-sight. This would imply Scl is on an almost radial or tangential orbit, but although the uncertainties are large, the existing proper motion measurements do not suggest either of these two hypotheses (Schweitzer et al. 1995; Piatek et al. 2006). All other inclinations should make tidal tails visible, however we do not detect any evidence of these in our data.

One can argue that the tidal tails are not visible because they have a low surface brightness and our photometric data are not deep enough to detect them. However, let us suppose the detected rotational signal from the spectroscopy is apparent rotation from faint tidal tails. We detect this signal with spectroscopically observed RGB stars, more luminous than $V = 20$. Our photometry is complete at ~ 2 magnitudes deeper than this, and shows the presence of many more stars than the selected RGB stars. Furthermore, our RGB stars classified as 3σ members from the spectroscopy represent only $\sim 15\%$ of the RGB stars in the photometry. Thus if we can detect a signal from our spectroscopy then we should have enough statistics to also be able to detect it in our photometry.

Another prediction from models of tidally disrupted dSphs to compare to the observations is the l.o.s. velocity gradient along the direction of orbital motion (e.g. Oh & Lin 1995; Klessen & Zhao 2002). The orbital direction on the sky is indicated by the proper motion. Since we detected a l.o.s. velocity gradient along the major axis of Scl, we would expect the direction of orbital motion to be aligned with the major axis if the detected signal is caused by tidal disruption. Figure 4.16 shows that neither of the two proper motion measurements suggests an alignment between the direction of Scl orbital motion and the detected signal, unless allowing for $\sim 2\sigma$ errors in the proper motion measurements.

From these arguments we conclude that it is unlikely that the detected velocity gradient along the major axis of Scl is a signature of tidal disruption, and thus it is likely to be due to real rotation.

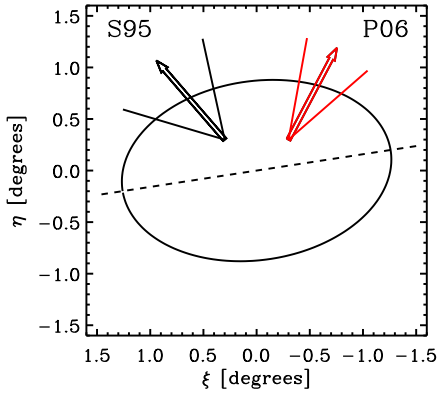

Figure 4.16: Schematic representation of the projected direction of Scl orbital motion from the existing proper motion measurements. The dark arrow at a P.A. = 39.94° (labelled as S95) indicates the measurement from Schweitzer et al. (1995), which derived a proper motion of (μ_α, μ_δ)=(36±22, 43±25) mas/century (corrected for the LSR and a Solar motion of (−9, +11, +7) km s^{-1} and assuming a distance of 8.5 kpc for the Sun from the Galactic centre). The light arrow at a P.A. = 332.9° (labelled as P06) indicates the measurement from Piatek et al. (2006) which derived a proper motion of (μ_α, μ_δ)=(−23±13, 45±13) mas/century (corrected for the LSR and a Solar motion of (−10.00, +5.25, +7.17) km s^{-1} and assuming a distance of 8.5 kpc for the Sun from the Galactic centre). The solid lines (black and red) are placed at the maximum position angle allowed by considering 1σ errors in both coordinates of the proper motion. The dashed line shows Scl projected major axis. If the rotation signal we detect in Scl is due to tidal disruption the proper motion is expected to align with the projected major axis direction.

If the detected signal is caused by rotation, then we can use the fitted value of the gradient to derive a lower limit of $v_{\rm rot,max} = 6$ km s^{-1} to the maximum rotational velocity (at $r = 0.8$ deg, the distance of our outermost bin along the major axis).

When rotation is responsible for the flattening of an axisymmetric galaxy, a simple relation holds between the true ellipticity of the galaxy and its v_0/σ_0 value, where v_0 is the mass weighted rotational velocity and σ_0 an estimate of the mass weighted velocity dispersion (Binney & Tremaine 1987). For a galaxy flattened by rotation and with an isotropic velocity ellipsoid, this relation does not vary much with the inclination of the galaxy with respect to the line-of-sight. In this case it is possible to replace v_0/σ_0 with the value measured along the line-of-sight $v_{\rm rot,los}/\sigma_{\rm los}$ (thus already mass/number weighted in resolved stellar populations studies) and consider the apparent ellipticity as the true one. Of course, we do not know either if Scl is an "isotropic rotator" nor its intrinsic inclination, however we are going to approximate v_0/σ_0 with $v_{\rm rot,los}/\sigma_{\rm los}$, which for Scl is ∼0.6.

The ratios expected for an "isotropic rotator" of a certain ellipticity are tabulated in Binney & Merrifield (1998), and for a galaxy of ellipticity 0.3 like Scl this ratio is

equal to 0.649. This means that the shape of Scl is consistent with being flattened by rotation, although due to the fact that Scl velocity ellipsoid and inclination are unknown, it is possible that velocity anisotropy is also contributing to the flattening of the galaxy.

The presence of actual rotation in Scl might give us important clues on the formation of dSphs. Mayer et al. (2001) proposed that rotationally supported galaxies such as dIrrs might transform into pressure supported systems such as dSphs through the tidal stirring exerted by the host galaxy, which in this case is the MW (see discussion in Chapter 3). Typically the predicted v_0/σ_0 for ellipticity similar to Scl is $\lesssim$0.5, comparable to the $v_{\rm rot,los}/\sigma_{\rm los} \sim 0.6$ measured in Scl. The efficiency of this transformation process is highly dependent on the orbital parameters of the satellite galaxies, i.e. pericentric distance and/or apocenter-to-pericenter ratio. It is thus expected that according to their orbital history some systems will suffer less from tidal stirring and might retain some of their original kinematic properties. One could expect the dSphs that are further away from the MW to show more evident signs of rotation. The marginal signal found in both Leo I and Leo II (Koch et al. 2007b,a) which have distances larger than 200 kpc could argue against this. However, their current location does not necessarily indicate that they were never close to the MW. As no proper motion measurements exist for these galaxies due to their large distance, it is possible that they are currently close to their apocenter, and/or are in a more radial orbit with respect to Scl, so that they suffered enough tidal stirring to erase the rotation signal. Once again more accurate proper motion measurements are necessary to make definitive statements.

4.5.2 Stellar population variations

Our DART photometric and spectroscopic surveys of the Scl and Fnx dSphs (Chapter 3) have highlighted important similarities and differences between these two galaxies.

The main similarity is the presence of multiple stellar components which are distinguishable in metallicity, spatial distribution and kinematics. In both cases, the metal rich stars are preferentially found in the central regions and have colder kinematics than the metal poor stars, which dominate in the outer regions.

Multiple stellar components might be a common characteristic of dSphs. Although, large surveys combining both photometric, velocity and metallicity measurements have not been carried out for many dwarf galaxies. Preliminary analysis of VLT/FLAMES data for the Sextans dSph (Battaglia et al. in preparation) shows the presence of a spatial variation in the metallicity but the kinematics of the MR and MP stars do not differ significantly. There is currently photometric evidence for stellar population gradients in Carina and Tucana (e.g., Harbeck et al. 2001), and a weak spectroscopically confirmed metallicity radial variation in Carina (Koch et al. 2006). For most of the discussion as to what could cause population gradients we refer to the discussion in Chapter 3. Here we speculate on some of the differences between Scl and Fnx.

The first striking difference is the age of the stellar components in Scl and Fnx. In Scl the multiple populations, both the MR and MP, are ancient (>10 Gyr old). In Fnx instead the MP component is as ancient as in Scl, but the MR component is between 2-8 Gyr old. Therefore it is clear that the differences between the various

stellar populations in Fnx have arisen on a longer timescale than in Scl.

Another major difference is that in Scl the majority of the stellar population is MP (and ancient), whilst in Fnx we have the opposite: the majority of Fnx stars are MR and have intermediate age. Assuming that MP stars formed in the earliest star formation epoch, this implies that the bulk of the star formation in Fnx occurred at intermediate epochs, around 2-8 Gyr ago, whilst in Scl there was apparently no gas left to form stars after the first star formation epoch.

If we also make the reasonable assumption that the different spatial distribution of MP/old and MR/younger stars reflects the distribution of the gas from which they formed (see also Chapter 3), it seems that the gas and/or metals were removed more efficiently from Scl than from Fnx, which managed to retain most of its gas/metals for subsequent star formation (assuming that Fnx did not accrete additional gas from external sources).

Several different mechanisms, such as supernovae explosions, tides and ram pressure, could be responsible for the higher removal efficiency of gas/metals from Scl. For example an higher number of SN might have exploded in Scl over a short time frame. This would affect the [α/Fe] vs [Fe/H] distribution, producing more α-enhanced stars in Scl at the low metallicity end, and shifting the "knee" of the distribution to higher [Fe/H] in Scl with respect to Fnx. The current data do not suggest such a difference (Letarte 2007; Hill et al. 2007; see also Chapter 2), however more HR data covering the low metallicity end of Fnx are needed to accurately test this. Also, supernovae explosions might have affected Scl more if it has a smaller potential well than Fnx. In favour of this hypothesis, there are indications that Fnx could be somewhat more massive than Scl (Walker et al. 2006; Battaglia et al. in preparation; see Chapter 5 for the mass determination of Scl). Simulations following the gas and metal evolution could give insights into the mass threshold needed to cause the observed differences. An alternative hypothesis is tides and ram pressure stripping (e.g., Mayer et al. 2006), in which case both the potential well and the orbital history of the objects would play a role. Less massive dSphs are more likely to be stripped of their gas, and so are dSphs with small pericenter distances and high apocenter-to-pericenter ratios. Consistent with this picture, Scl appears to have an orbital period of $\sim$ 2 Gyr and a pericenter of $\sim$ 70 kpc (Piatek et al. 2006) with respect to the longer orbital period of Fnx, which is 4-5 Gyr, and the larger pericenter, $\sim$ 120 kpc. However, when taking into account the uncertainties in the proper motion measurements, the orbital parameters for these two galaxies overlap, making more definitive conclusions difficult.

In reality it is most likely that a combination of several mechanisms is responsible for the changes in the behaviour of stellar populations with time. Studies of isolated dSphs would be useful in order to distinguish between these effects. Objects like Tucanae for example were probably never close enough to a large galaxy to have suffered from either tidal or ram pressure stripping. The presence of stellar population gradients in isolated dSphs would argue against environmental effects as a possible cause. More observations of a similar nature to the ones presented here are needed for a large number of dSphs and more distant to study the effect of the environment on their detailed chemo-dynamical properties. The large aperture telescopes such as Magellan, VLT and Keck equipped with wide area CCD cameras and multi-fibres spectrographs like FLAMES, MIKE and DEIMOS make this a feasible task for all Milky Way satellites, requiring only 2-3 nights

observing time in order to derive accurate velocities and CaT metallicities for hundreds of RGB stars out to the tidal radius.

4.6 Summary and conclusions

We have undertaken the most complete and accurate survey of the Scl dSph out to and beyond the nominal tidal radius, combining ESO/WFI photometry with VLT/FLAMES low resolution spectroscopy to study in detail the spatial and chemo-dynamical properties of the resolved stellar population of this galaxy.

From our photometry we studied the spatial distribution of Scl stars of different ages/ metallicities as selected from the CMD. We find that the BHB stars, older/metal poor, have a less centrally concentrated and more extended distribution than the RHB stars, which are younger/more metal rich. The RHB stars follow a Sersic profile with scale radius $R_S[']=7.7\pm0.9$ and shape parameter $m=0.74\pm0.07$; the BHB stars follow a Plummer profile with $b[']=15.1\pm0.5$.

As in previous works we find that the overall density surface profile of Scl is not well represented by a single component fit because it shows hints of a "break population" at radii $r>0.7$deg, which has been interpreted in previous studies as a sign of tidal disturbance. However our new data show that this "break population" is most likely due to the fact that Scl hosts two stellar populations with different spatial distributions, and thus it is necessary to fit the overall profile with the sum of these two components.

From our VLT/FLAMES low resolution (R$\sim$6500) spectroscopy in the CaT region we derived accurate velocities ($\pm$ 2 km s^{-1}) and metallicities ($\pm$0.1 dex) for $\sim$ 650 RGB stars. A simple kinematic selection gives 470 probable members of Scl from this sample.

The resulting metallicity distribution function shows a wide metallicity range, $-3.0\lesssim$ [Fe/H] $\lesssim-0.7$, and is well approximated by the sum of a MR and a MP component. The first one peaks at [Fe/H]$=-1.5$ with dispersion 0.2 dex, and the latter peaks at [Fe/H]$=-2.0$ with dispersion 0.26 dex. These two components have different spatial distributions and kinematics, with the more MR stars found predominantly in the central regions of the galaxy and having a colder kinematics, and the more MP stars found everywhere. This variation happens on the same spatial scale as the RHB/BHB swap of dominance, hinting at the fact that MR stars are associated to RHB and the MP stars to the BHB.

We can thus distinguish in Scl two stellar components according to their spatial, metallicity and kinematics properties. Determination of the age of these stars is necessary to understand on which time scale such differences have arisen.

Our spectroscopic analysis of Scl shows that the kinematics of this galaxy is consistent with a velocity gradient of $7.6^{+3.0}_{-2.2}$ km s^{-1} deg^{-1} along the projected major axis. We interpret this signal as rotation around the minor axis, which makes Scl the only dSph of the MW system in which statistically significant rotation has been measured.

Another finding of our spectroscopic survey is the presence of a cold structure, which might be the remnant of a dissolved stellar cluster.

The data presented here show that a wealth of information on dSphs might be missed leading to inaccurate conclusions when limiting the analysis of these objects to

a small region or aspect. Combining photometry and spectroscopic follow up over a large field has proved to be crucial to obtain an accurate picture of these surprisingly complex small galaxies.

References

Azzopardi, M., Lequeux, J., & Westerlund, B. E. 1986, A&A, 161, 232

Binney, J. & Merrifield, M. 1998, Galactic astronomy (Galactic astronomy / James Binney and Michael Merrifield. Princeton, NJ : Princeton University Press, 1998. (Princeton series in astrophysics) QB857 .B522 1998)

Binney, J. & Tremaine, S. 1987, Galactic dynamics (Princeton, NJ, Princeton University Press, 1987, 747 p.)

Blecha, A., North, P., Royer, F., & Simond, G. 2003, VLT-SPE-OGL-13730-0040

Clementini, G., Ripepi, V., Bragaglia, A., Fiorenzano, A. F. M., Held, E. V., & Gratton, R. G. 2005, MNRAS, 363, 734

Coleman, M. G., Da Costa, G. S., & Bland-Hawthorn, J. 2005, AJ, 130, 1065

Dehnen, W. & Binney, J. J. 1998, MNRAS, 298, 387

Demers, S., Krautter, A., & Kunkel, W. E. 1980, AJ, 85, 1587

Eskridge, P. B. 1988a, AJ, 95, 1706

—. 1988b, AJ, 96, 1336

Frogel, J. A., Blanco, V. M., Cohen, J. G., & McCarthy, M. F. 1982, ApJ, 252, 133

Geha, M., Guhathakurta, P., & van der Marel, R. P. 2003, AJ, 126, 1794

Groenewegen, M. A. T. 2002, ArXiv Astrophysics e-prints

Harbeck, D., Grebel, E. K., Holtzman, J., Guhathakurta, P., Brandner, W., Geisler, D., Sarajedini, A., Dolphin, A., Hurley-Keller, D., & Mateo, M. 2001, AJ, 122, 3092

Hargreaves, J. C., Gilmore, G., & Annan, J. D. 1996, MNRAS, 279, 108

Hargreaves, J. C., Gilmore, G., Irwin, M. J., & Carter, D. 1994, MNRAS, 271, 693

Hurley-Keller, D., Mateo, M., & Grebel, E. K. 1999, ApJ, 523, L25

Illingworth, G. 1976, ApJ, 204, 73

Irwin, M. & Hatzidimitriou, D. 1995, MNRAS, 277, 1354

Kaluzny, J., Kubiak, M., Szymanski, M., Udalski, A., Krzeminski, W., & Mateo, M. 1995, A&AS, 112, 407

King, I. 1962, AJ, 67, 471

Klessen, R. S. & Kroupa, P. 1998, ApJ, 498, 143

Klessen, R. S. & Zhao, H. 2002, ApJ, 566, 838

Kleyna, J. T., Wilkinson, M. I., Gilmore, G., & Evans, N. W. 2003, ApJ, 588, L21

Koch, A., Grebel, E. K., Wyse, R. F. G., Kleyna, J. T., Wilkinson, M. I., Harbeck, D. R., Gilmore, G. F., & Evans, N. W. 2006, AJ, 131, 895

Koch, A., Kleyna, J. T., Wilkinson, M. I., Grebel, E. K., Gilmore, G. F., Evans, N. W., Wyse, R. F. G., & Harbeck, D. R. 2007a, AJ, 134, 566

Koch, A., Wilkinson, M. I., Kleyna, J. T., Gilmore, G. F., Grebel, E. K., Mackey, A. D., Evans, N. W., & Wyse, R. F. G. 2007b, ApJ, 657, 241

Kroupa, P. 1997, New Astronomy, 2, 139

Majewski, S. R., Siegel, M. H., Patterson, R. J., & Rood, R. T. 1999, ApJ, 520, L33

Mateo, M. L. 1998, ARA&A, 36, 435

Mayer, L., Governato, F., Colpi, M., Moore, B., Quinn, T., Wadsley, J., Stadel, J., & Lake, G. 2001, ApJ, 559, 754

Mayer, L., Mastropietro, C., Wadsley, J., Stadel, J., & Moore, B. 2006, MNRAS, 369, 1021

Monkiewicz, J., Mould, J. R., Gallagher, III, J. S., Clarke, J. T., Trauger, J. T., Grillmair, C., Ballester, G. E., Burrows, C. J., Crisp, D., Evans, R., Griffiths, R., Hester, J. J., Hoessel, J. G., Holtzman, J. A., Krist, J. E., Meadows, V., & Scowen, P. A. 1999, PASP, 111, 1392

Muñoz, R. R., Majewski, S. R., Zaggia, S., Kunkel, W. E., Frinchaboy, P. M., Nidever, D. L., Crnojevic, D., Patterson, R. J., Crane, J. D., Johnston, K. V., Sohn, S. T., Bernstein, R., & Shectman, S. 2006, ApJ, 649, 201

Oh, K. S., Lin, D. N. C., & Aarseth, S. J. 1995, ApJ, 442, 142

Olszewski, E. W., Pryor, C., & Armandroff, T. E. 1996, AJ, 111, 750

Pasquini, L., Avila, G., Blecha, A., Cacciari, C., Cayatte, V., Colless, M., Damiani, F., de Propris, R., Dekker, H., di Marcantonio, P., Farrell, T., Gillingham, P., Guinouard, I., Hammer, F., Kaufer, A., Hill, V., Marteaud, M., Modigliani, A., Mulas, G., North, P., Popovic, D., Rossetti, E., Royer, F., Santin, P., Schmutzer, R., Simond, G., Vola, P., Waller, L., & Zoccali, M. 2002, The Messenger, 110, 1

Piatek, S., Pryor, C., Bristow, P., Olszewski, E. W., Harris, H. C., Mateo, M., Minniti, D., & Tinney, C. G. 2006, AJ, 131, 1445

Plummer, H. C. 1911, MNRAS, 71, 460

Pryor, C., McClure, R. D., Fletcher, J. M., & Hesser, J. E. 1988, in IAU Symposium, Vol. 126, The Harlow-Shapley Symposium on Globular Cluster Systems in Galaxies, ed. J. E. Grindlay & A. G. D. Philip, 661

Robin, A. C., Reylé, C., Derrière, S., & Picaud, S. 2003, A&A, 409, 523

Schweitzer, A. E., Cudworth, K. M., Majewski, S. R., & Suntzeff, N. B. 1995, AJ, 110, 2747

Sersic, J. L. 1968, Atlas de galaxias australes (Cordoba, Argentina: Observatorio Astronomico, 1968)

Shetrone, M., Venn, K. A., Tolstoy, E., Primas, F., Hill, V., & Kaufer, A. 2003, AJ, 125, 684

Shetrone, M. D., Briley, M., & Brewer, J. P. 1998, A&A, 335, 919

Tolstoy, E., Irwin, M. J., Cole, A. A., Pasquini, L., Gilmozzi, R., & Gallagher, J. S. 2001, MNRAS, 327, 918

Tolstoy, E., Irwin, M. J., Helmi, A., Battaglia, G., Jablonka, P., Hill, V., Venn, K. A., Shetrone, M. D., Letarte, B., Cole, A. A., Primas, F., Francois, P., Arimoto, N., Sadakane, K., Kaufer, A., Szeifert, T., & Abel, T. 2004, ApJ, 617, L119

Tolstoy, E., Venn, K. A., Shetrone, M., Primas, F., Hill, V., Kaufer, A., & Szeifert, T. 2003, AJ, 125, 707

van den Bergh, S. 2006, AJ, 131, 304

Walcher, C. J., Fried, J. W., Burkert, A., & Klessen, R. S. 2003, A&A, 406, 847

Walker, M. G., Mateo, M., Olszewski, E. W., Bernstein, R., Wang, X., & Woodroofe, M. 2006a, AJ, 131, 2114

Walker, M. G., Mateo, M., Olszewski, E. W., Pal, J. K., Sen, B., & Woodroofe, M. 2006b, ApJ, 642, L41

Westfall, K. B., Majewski, S. R., Ostheimer, J. C., Frinchaboy, P. M., Kunkel, W. E., Patterson, R. J., & Link, R. 2006, AJ, 131, 375

Wilkinson, M. I., Kleyna, J. T., Evans, N. W., Gilmore, G. F., Irwin, M. J., & Grebel, E. K. 2004, ApJ, 611, L21